Journal of Materials Chemistry C

ROYAL SOCIETY OF CHEMISTRY

PAPER

View Article Online
View Journal | View Issue

Cite this: J. Mater. Chem. C, 2025, 13, 16981

The importance of accounting for non-radiative decay when screening materials for singlet fission: the case of Pigment Red 254†

Daniel Z. Hook, [a] Rachel Kilbride,[b] Daniel J. Gillard,[a] Samara Medina Rivero,[ac] Ravi Kumar Venkatraman, [a] James P. Pidgeon,[a] Alexander Tartakovskii[a] and Jenny Clark *[a]

Singlet exciton fission (SF) is a process in which two triplet (spin-1) excitons are generated in a material for every absorbed photon. If properly harnessed, SF could increase photovoltaic efficiency beyond the single-junction thermodynamic limit, from ≈30% to >40%. However, to date no solid-state SF sensitiser has proven ideal for this application. To solve this problem, recent work using quantum chemical calculations to screen materials deposited in the Cambridge crystallographic database [D. Padula, O. H. Omar, T. Nematiaram and A. Troisi, *Energy Environ. Sci.*, 2019, **12**, 2412–2416] has identified several candidates. Of them, Pigment Red 254, a common automotive dye pigment, appears an ideal candidate, with the correct energetics, crystal structure, stability, absorption properties and cost. Here we use steady-state and transient spectroscopy of films of Pigment Red 254 to test for the presence of SF. We find that rapid picosecond non-radiative decay out-competes SF, re-populating the ground-state within 20–40 ps. The rapid non-radiative decay is orders of magnitude faster than expected from Jortner's empirical gap laws. Further, we perform TRIR spectroscopy to investigate which molecular vibrations mediate this decay, and find high infra-red activity in the hydrogen bonds that form between molecules in the solid state. We propose a model for proton transfer mediated by a conical intersection with the ground state of an alternate molecular conformer. Our results highlight the importance of including non-radiative decay in calculations aimed at screening molecules for photonic or energy applications.

Received 28th March 2025,
Accepted 10th July 2025

DOI: 10.1039/d5tc01336d

rsc.li/materials-c

1 Introduction

Singlet fission (SF) is a form of multiexciton generation in which one singlet exciton can produce two triplet excitons.[1] Generating two lower energy triplets per photon could overcome thermalisation losses in solar cells if properly harnessed. Therefore, SF sensitised devices could bypass the fundamental single-junction thermodynamic limit, increasing the maximum achievable efficiency of solar cells from 33.7% to ∼45%.[2,3]

However, the library of existing molecules which exhibit SF is limited,[4] and none are yet suitable for solar cell applications. In addition to simply undergoing SF, candidate materials must have:[2] (1) good stability in oxygen-rich, humid, high fluence environments; (2) strong absorption in the visible region of the solar spectrum; (3) high triplet mobility and lifetime; (4) favourable triplet pair dissociation rates; and (5) triplet energies corresponding to efficient photovoltaic semiconductor band-gap energies (*e.g.* silicon). To these we add an additional condition: (6) facile synthesis and the possibility of cheap mass-production.

The process of experimentally screening materials for SF and properties (1)–(6) is slow. To expedite this process, Padula *et al.*[5] developed an algorithm that uses time-dependent density functional theory (TD-DFT) to screen the Cambridge Crystallographic Database for solid-state materials that satisfy the basic criteria for SF: $E(S_1) > 2 \times E(T_1)$ and $E(T_2) > 2 \times E(T_1)$, where $E(S_1)$ is the energy of the first singlet excited state (S_1) and $E(T_i)$ is the energy of the ith triplet state. The latter condition prevents intersystem crossing to a higher triplet state from occurring as a loss pathway.

One predicted result that shows exceptional stability, high absorption in the visible region, a predicted triplet energy of

[a] Department of Physics and Astronomy, University of Sheffield, S3 7RH, UK. E-mail: danhook42@outlook.com, jenny.clark@sheffield.ac.uk, a.tartakovskii@sheffield.ac.uk
[b] Department of Chemistry, University of Sheffield, Sheffield S3 7HF, UK
[c] Department of Physical Chemistry, University of Málaga Andalucia-Tech Campus de Teatinos s/n, 29071 Málaga, Spain

† Electronic supplementary information (ESI) available. See DOI: https://doi.org/10.1039/d5tc01336d

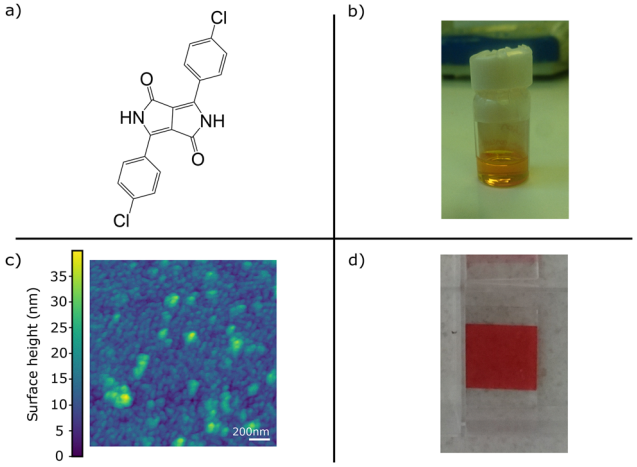

Fig. 1 Samples of Red 254. (a) Molecular structure of Red 254. (b) Sample image of Red 254 in solution of DMSO, (c) atomic force microscopy (AFM) plot of thermally evaporated thin films of Red 254 on quartz-coated glass. These films are visibly polycrystalline, with a height of 38.87 nm and an RMS roughness of 12.75 nm and (d) sample image of Red 254 as a evaporated thin film on quartz-coated glass. The hypsochromic shift as the change in colour in solution *vs.* solid states is easily visible; the solution transmits yellow light, whereas the solid predominantly transmits red light.

1.20 eV, suitable for use with silicon, and that is already mass-produced for commercial purposes is 4-bis(4-chlorophenyl)-2, 5-dihydropyrrolo[3,4-*c*]-pyrrole-3,6-dione, also known as Pigment Red 254, p-Cl-DPP or Ferrari red (see Fig. 1). In this work, this dye will be referred to as Red 254. Red 254 is a diketopyrrolopyrrole-based dye (see structure in Fig. 1(a)) that is famously stable in hot, bright, humid environments; sufficiently so to be used as a pigment in car paint.[6–10]

However, despite these excellent properties, and its favourable calculated energies for SF,[5] the excited-state dynamics of Red 254 have not been comprehensively investigated. Here we investigate the photophysical properties of Red 254 for its potential as a SF sensitiser. This work tests whether Padula *et al.*'s algorithm has sufficient information to predict SF capability.

We note that molecules with a similar diketopyrrolopyrrole (DPP) core have been studied[9,11–16] and show evidence of SF.[14–16] However, these molecules have been designed to be solution-processable (Red 254 is insoluble in most organic solvents[9,12,17,18]). Such custom synthesis is generally expensive and can be difficult to scale up. Should it exhibit singlet fission, Red 254 has potential to be more rapidly deployable as a SF sensitiser, at significantly lower cost, because it is already mass produced, and it can be formed into films by evaporation, currently the technology of choice for most large-scale (opto)-electronics.[19]

Here we demonstrate that evaporated thin films of Red 254 are only weakly emissive and show long lived signals in transient absorption spectroscopy measurements. However, through careful analysis of the data, we demonstrate that these long-lived features are due to thermal artefacts arising from rapid (picosecond) non-radiative decay of photo-excitations to the ground state. In other words, we see no evidence of SF in Red 254 films.

We further investigate using Fourier transform infra-red and time-resolved infra-red spectroscopy to find evidence of signal linked with nitrogen–hydrogen and carbon double-bond stretching modes associated with the non-radiative decay process, indicating decay *via* a proton-transfer type charge transfer state. We propose a model for this process linking the time-scales observed in the time-resolved spectra to each step in the decay process.

2 Results

2.1 UV-Vis characterisation

Due to the strong intermolecular hydrogen bonding in Red 254,[13,20] solution processing solid films is not preferred. Here we study thin films made by thermal evaporation full details of which can be found in the methods section. An atomic force microscopy (AFM) image of a typical film in Fig. 1(c) indicates that films produced in this way are strongly crystalline, with grains on the order of tens of nanometres. The photograph of a film in panel (d) shows that the film is homogeneous and strongly absorbing.

Fig. 2 shows the steady state absorption and emission spectra of Red 254, both in solution of DMSO (top), and in a sublimated thin film on a quartz-coated glass substrate (bottom). The energy of the 0-0 peak maxima are shown in Table 1 and compared with calculated values.[5] These spectra are compared to the UV-vis absorption and emission spectra of a sublimated thin film of Red 254 on a sapphire substrate in Fig. S5 (ESI†). There it is seen that the emission spectra differ only slightly from the emission from the glass substrate sample, while the absorption spectrum shows some marked differences, with the vibrational peaks being relatively less intense than the 0-0 peak, and the presence of a more intense tail in the sapphire substrate sample. This indicates a small environment-dependent change to the absorption characteristics, through peak broadening or peak intensity. However, the location of the absorption maximum does not change, indicating that the differences are primarily vibrational, either through a sample-dependent change in morphology or some sample–substrate interaction. In solution, we observe a Stokes shift of 61 meV and the emission and absorption spectra show similar vibronic structure.

The absorption and emission spectra of isolated molecular emitters can usually be fitted using the standard Franck–Condon progression in eqn (3) (see Köhler and Bässler[21] for details)

$$I(\hbar\omega) = [n(\hbar\omega)\cdot\hbar\omega]^k \cdot \sum_{m_j}\prod_j \frac{S_j^{m_j}}{m_j!}\mathrm{e}^{-S_j} \times \Gamma\cdot\delta\left(\hbar\omega - \left(\hbar\omega - K\cdot\sum_j m_j\hbar\omega\right)\right)$$

where $\hbar\omega$ is the photon energy, $\hbar\omega_0$ is the 0-vibration electronic transition energy (also known as the 0-0 transition energy), $\hbar\omega_j$ is

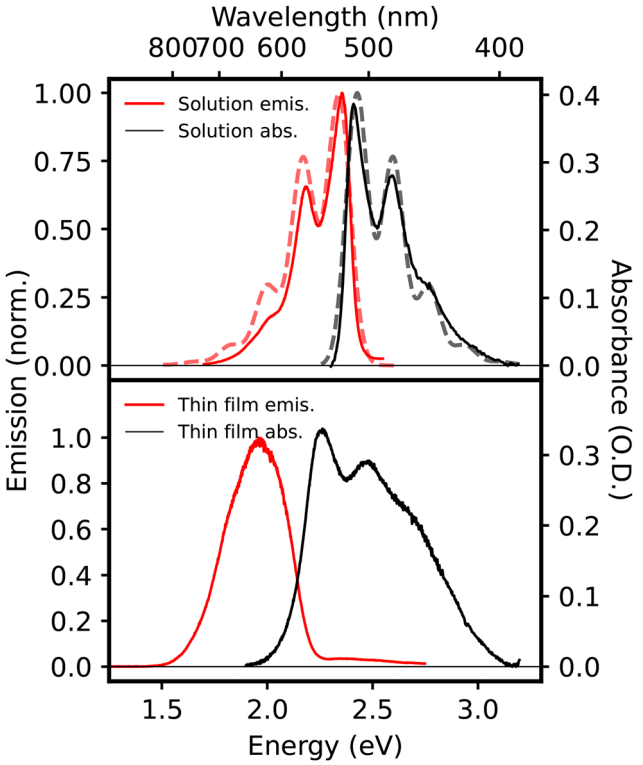

Fig. 2 Steady state spectroscopic characterisation of Red 254. UV-Vis absorption and emission spectra of a solution phase sample of Red 254 in DMSO (top) and absorption and emission spectra of sublimated thin films of Red 254 on a quartz-coated glass substrate (bottom). The emission spectra of both samples were taken with an excitation of 405 nm. The dashed line plots overlaid with the solution-phase spectra are Franck–Condon fits to the data, full details of which are displayed in the main body of text, as well as in Fig. S3 and S4 (ESI†) and in Table 2.

Table 1 Vertical (absorption, Abs.) and adiabatic (emission, Em.) transition energies of the lowest-lying singlet (S_1) of Red 254 in the solution or solid phases compared with calculated values.[5] Experimental values are from Fig. 2 at the energy of maximum absorption/emission intensity

	Solution S_1	Solid S_1	Calc. S_1	Calc. T_1
Abs. energy (eV)	2.41	2.26	2.415	1.203
Em. energy (eV)	2.35	1.959		

the energy of a vibrational normal mode labelled j, which has a quantum occupation number of m_j (for example the 0-1 transition for a particular normal mode has $m_j = 1$). S_j is the Huang–Rhys factor for vibrational normal mode j. S_j is a measure of the coupling strength between the electronic transition and the vibrational normal mode j, and is proportional to the square of the shift of the normal coordinate displacement between the ground and excited state potential energy surface $S_j \propto \Delta Q_j^2$ and to the intensity of the resonance Raman peak for mode j. To reduce the number of fitting parameters, the energies of the vibrational normal modes can be fixed to the values determined from resonance Raman spectroscopy. The Franck–Condon fit is shown together with the UV-vis spectra in Fig. 2, with further details and the resonance Raman spectrum used shown in Fig. S3, S4 and S2 (ESI†) respectively. Γ is a lineshape function, taken to be Gaussian to account for coupling to low energy vibrations and dynamic and static disorder. $n(\hbar\omega)$ is the energy-dependent refractive index of the material and is included to accurately account for the photon density of states *via* $[n(\hbar\omega)\cdot\hbar\omega]^k$, where $k = 3$ for emission spectra and $k = 1$ for absorption (due to the electric field interacting with the sample multiple times, according the the Einstein relations). For solution samples, n does not vary significantly with photon energy and is assumed to be constant (this is not true for solid films). Finally, we set $K = -1$ for emission and +1 for absorption, as the energy of $m_j \neq 0$ transitions is lower for emission and higher for absorption.[21]

Using this equation, and fixing the vibrational mode energies to two effective modes obtained from resonance Raman spectroscopy (see eqn (3) in the Methods section and Table 2), and letting all other parameters vary freely, the experimental spectra can be fit using a least-squares fitting algorithm, as described in the methods section.[22] The solution absorption spectrum in Fig. 2 (top) was fitted first and, subsequently fixing the Huang–Rhys parameters, the emission spectrum was fitted. The resultant fits are shown by the dashed lines in Fig. 2 and the fitting parameters are shown in Table 2. The fits show a slight reduction in Huang–Rhys parameter following excited-state relaxation. The reasonable fit of both absorption and emission spectra to a standard Franck–Condon progression allows us to conclude that Red 254 in solution behaves as a standard molecular emitter with no obvious signs of tautomers, aggregation, charge-transfer or other unusual photophysical behaviour.

Fig. 2 (bottom) shows the absorption and emission spectra of a evaporated film of Red 254 on quartz-coated glass. Compared with solution, the absorption maximum is shifted by 0.15 eV and the spectrum cannot be fitted with a Franck–Condon progression using the vibrational energies extracted from the resonance Raman spectrum. Due to the presence of similar behaviour predicted and observed in diketopyrrolopyrrole derivatives, we can assign this shift to π–π out-of-plane interactions between adjacent molecules in the excited state.[14,23,24] In addition, the large shift of the absorption maximum may have some contribution from a strengthening of the intermolecular hydrogen bonding in the solid state.[25]

The emission yield in the thin film is significantly lower than the solution emission (the film emission was almost unmeasurable on our setup, despite the strong absorption, and and is relatively featureless with a tail extending to energies above the absorption edge at 2.2 eV). The low emission yield indicates the presence of a non-emissive pathway for excited

Table 2 Franck–Condon fitting parameters for Red 254 steady-state solution absorption (Abs.) and emission (Em.) spectra in Fig. 2 values presented with an asterisk (*) indicate fitting parameters that were allowed to vary freely

	$\hbar\omega_0$	$\hbar\omega_{j=1}$	$\hbar\omega_{j=2}$	$S_{j=1}$	$S_{j=1}$
Solu. Abs	2.426*	0.195	0.166	0.115*	0.662*
Solu. Em	2.339*	0.195	0.166	0.115	0.662

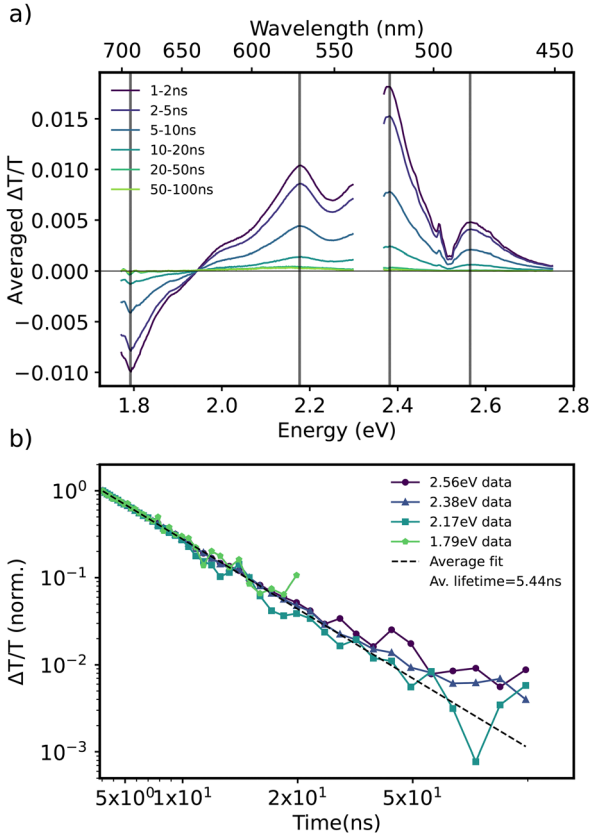

Fig. 3 Nanosecond scale transient absorption (a) spectra and (b) kinetics of solution of Red 254 in solution of DMSO. The energies used for the kinetics are marked by vertical lines on subplot (a). The kinetics are well fit by a mono-exponential decay with a lifetime of 5.44 ± 0.016 ns, representing the emissive lifetime of the Red 254 monomer. The pump wavelength used for this experiment was 532 nm, with a pump power of 2 mW.

state decay in the solid film. The apparently large Stokes shift of 330 meV combined with the lack of symmetry with the absorption spectrum suggests that the detected emission takes place from a different state than the state depicted in the absorption spectrum. Furthermore, we cannot exclude the possibility for this effect being enhanced by self-absorption due to waveguiding of light in the film. The fact that the tail extends to higher energies may indicate that some the emission we measure occurs rapidly, before the excited state population can undergo vibrational relaxation.

To test whether the significant non-radiative decay in Red 254 thin films is due to SF, we used transient absorption spectroscopy to investigate its time-dependent excited state dynamics. As a control, we first measured the dilute solution of Red 254 in DMSO, shown in Fig. 3. The solution-phase transient absorption spectra are dominated by features from the S_1 population: the positive features correspond to ground-state bleach (GSB) and stimulated emission (SE) (they are overlapped with the ground-state absorption and fluorescence spectra in Fig. 1(a), see Fig. S7, ESI†).

The negative feature, peaking at 1.8 eV is an $S_1 \rightarrow S_n$ excited-state absorption feature, evidenced by the presence of an isosbestic point at $\Delta T/T = 0$ around 1.95 eV. The normalised kinetics of Red 254 in solution shown in Fig. 3(b) decay mono-exponentially (τ = 5.44 ± 0.016 ns). We conclude that in solution we observe only singlet decay with no evidence of triplets, tautomerization or other excited-state decay pathways.

Compared with the simplicity of the solution TA spectra/dynamics, the solid Red 254 shows more complex TA spectroscopic behaviour. Fig. 4 (left) shows the TA spectra of a Red 254 evaporated thin film on quartz-coated glass substrate, on picosecond timescales (top) and on nanosecond timescales (bottom). The right panels of the figure show similar data with the film evaporated on a sapphire substrate. At early times (~10–100 ps), similar to the solution spectra in Fig. 3(a), the spectra show positive GSB features (matching the steady state absorption spectrum), and a negative feature at <2.00 eV that we assign to $S_1 \rightarrow S_n$ ESA. This ESA decays on a tens of picosecond timescale, indicating an S_1 lifetime over two orders of magnitude shorter than in solution (compare Fig. 3 with Fig. 5 and the lifetimes in Table 1). There is no visible SE feature even at the earliest times, possibly due to overlapping ESA. The slight differences between the TA data on quartz and sapphire will be described below. At longer times (bottom panels, ~2 ns–3 μs) the spectra evolve, demonstrating long-lived spectral features with apparent ESA overlapped with the GSB (evident at ~2.1 eV and at ~2.6 eV). Interestingly, the dynamics shown in Fig. 5 on these timescales are highly substrate dependent, with the signal decaying significantly faster on the sapphire substrate.

While a short-lived (10 s of picoseconds) S_1 lifetime, long-lived ns μs^{-1} TA signals and low fluorescence yield could indicate SF, the fact that we observe different decay dynamics on the two different substrates (quartz-coated glass, sapphire), suggests that the long-lived features we observe are due to thermal effects, similar to those reported in Albert-Seifried and Friend[26] and Rao *et al.*[27] In this case, the differences in TA dynamics between the films on quartz-coated glass and sapphire substrates can be attributed to the fact that sapphire has a thermal conductivity ~24 times that of quartz.[28] The more rapid decay on sapphire compared with glass can therefore be attributed to more rapid dissipation of heat from the film.

To test this heating artefact hypothesis, we measured the temperature dependence of the ground state absorption of the thin film samples of Red 254 and compare it with the shape of the long-lived TA spectra. This is shown in Fig. 6, for both the quartz substrate sample (top) and the sapphire substrate sample (bottom). These plots were generated by taking the steady state absorption of the sample both at room temperature, and when heated to a range of temperatures shown in Table S1 (ESI†). These heated ground state absorption spectra were subtracted from the room temperature spectrum. This is plotted together with the transient absorption spectra of the quartz and sapphire substrate for comparison. The resultant difference spectra from the heated ground state absorption accurately reproduce the nanosecond transient absorption spectra, confirming that the long-lived transient absorption features result from a hot ground state.[26,27]

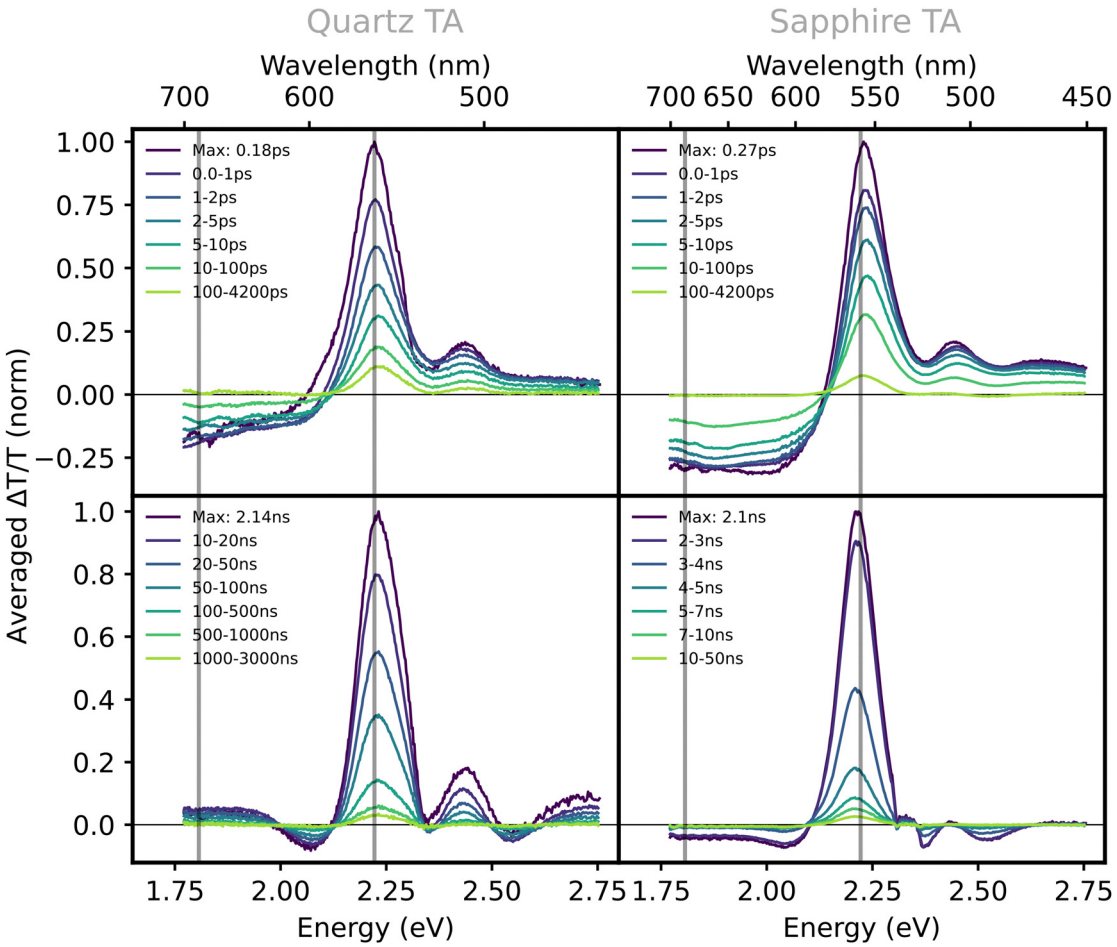

Fig. 4 Transient absorption spectra of evaporated thin films of Red 254 on quartz (left) and sapphire (right) at picosecond (top) and nanosecond (bottom) timescales with 532 nm excitation. The energies from which the kinetics (Fig. 5) were taken are shown on this figure as grey vertical lines.

As this hot ground state signal is the dominant origin of the long-lived (ns μs^{-1}) signals in the TA data, we conclude that we see no evidence of triplet formation *via* SF in these thin films. Instead, the primary photoexcited state, S_1 decays rapidly (10 s of picoseconds). The lack of fluorescence and the heating artefacts in the TA spectroscopy data suggests that S_1 decays non-radiatively to the ground-state. This rapid non-radiative S_1 decay is significantly faster the radiative decay in solution (5.44 ns). We hypothesize that this rapid non-radiative decay out-competes SF and is the reason for the lack of measurable SF in these samples.

Such rapid non-radiative decay is unlikely to be due to the usual non-radiative decay channels, typically governed by Jortner's empirical 'gap-law of non-radiative decay'.[29] Jortner's gap law applies in the limit of weak interstate coupling (a small displacement of the excited state potential energy surface from the ground state surface, ΔQ), and in such cases the non-radiative decay rate is given by

$$k_{\mathrm{nr}} \propto \exp\left(-\frac{\gamma \Delta E}{\hbar \omega_M}\right), \quad (1)$$

where $\hbar\omega_M$ is the energy of a given transition-active vibrational mode M, γ is a parameter referred to as the coupling coefficient, and ΔE is the energy gap between the initial and final states.[29] In other words, as the energy gap increases, the radiative rate falls off exponentially.

Fig. 7 shows the non-radiative decay rate of several diketopyrrolopyrrole (DPP) derivatives[23,30–32] that are structurally similar to Red 254. They follow a consistent transition energy-lifetime relation according approximately to an exponential gap-law dependence (dashed line). However the non-radiative decay rate of Red 254 in solid form is ∼900 times faster than predicted by the gap-law relationship. This suggests that non-radiative decay in Red 254 may occur *via* strong (large ΔQ) interstate coupling between the first excited- and ground-state potential energy surfaces,[29] rather than a non-adiabatic transition between weakly coupled states.

Research into non-radiative decay in diketopyrrolopyrroles has been limited, especially in the solid state. This lack of research has been driven by the difficulty of dissolving and film-processing the unsubstituted diketopyrrolopyrrole dye,[9,11–13,17,18] as well as different properties of the versatile diketopyrrolopyrrole molecule and its derivatives taking the focus of research. These include singlet fission, as has been previously discussed,[14,15,33] and the high fluorescence of some N–H substituted derivatives in the long wavelength region of the visible spectrum.[11,23,34]

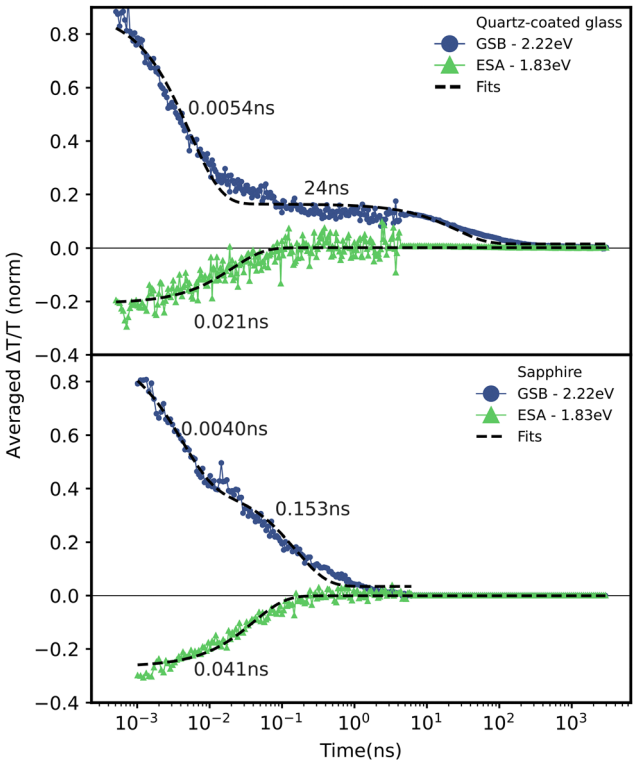

Fig. 5 Transient absorption kinetics of evaporated thin films of Red 254 on quartz (top) and sapphire (bottom) substrates, with the data from picosecond and nanosecond timescales combined. The nanosecond-scale data has been normalised to its overlap with the picosecond-scale data. The kinetics of the two energies shown correspond to the primary peak of the GSB in the TA signal (2.22 eV) and the low-energy ESA feature (1.83 eV). While the ESA features can be fit with monoexponential decays with lifetimes of 21 ± 1.6 ps (quartz) and 41 ± 1.5 ps (sapphire), the GSB feature's decays are best reproduced by a biexponential decay with the quartz decay having lifetimes of 5.4 ± 0.16 ps and 24 ± 3.2 ns and the sapphire substrate sample having a decay with lifetimes of 4.1 ± 0.3 ps and 154 ± 9.3 ps.

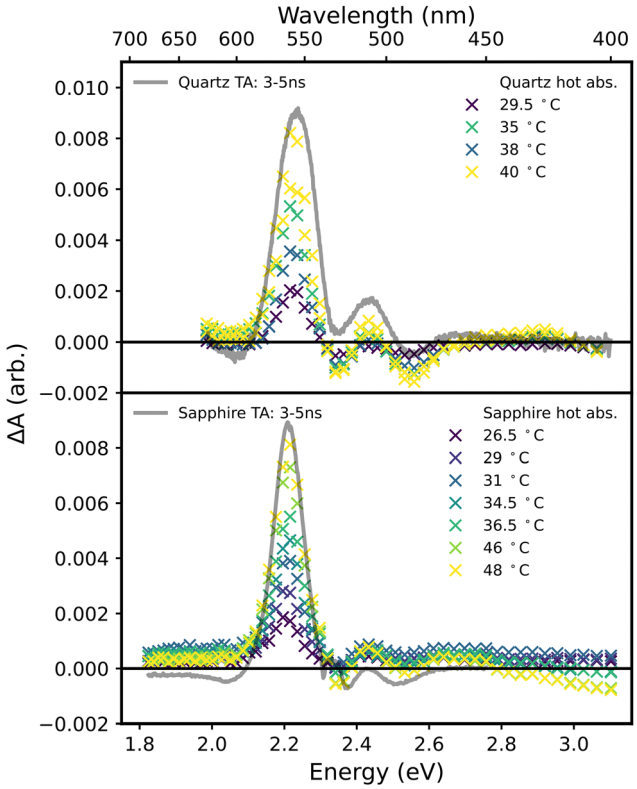

Fig. 6 Temperature dependent difference spectra of evaporated thin film of Red 254 on a quartz (top) and a sapphire substrate (bottom). The maxima of the nanosecond transient absorption spectra as indicated in Fig. 4 (2.1 ns) are plotted on alongside their respective difference spectra to illustrate that the features of the TA spectra are reproduced by these difference spectra, as well as the differences between the quartz and sapphire substrates.

2.2 Infra-red characterisation

Here we have demonstrated that in a poly-crystalline thin film, Pigment Red 254 undergoes a rapid non-radiative decay that is not exhibited in the solution phase. We have shown that this non-radiative decay out-competes any potential singlet fission or triplet generation processes as well as radiative or gap-law mediated non-radiative decay, granting it its short excited state lifetime.

While this short decay lifetime does prevent the formation of long-lived excited states, we have demonstrated that this non-radiative decay does not proceed *via* a typical non-adiabatic process, which is itself of interest. Understanding the mechanism behind the non-radiative decay in Red 254 is desirable to facilitate the intelligent engineering of future molecules, both to prevent non-radiative decay as a loss mechanism where a long-lived or radiative electronic excited state is preferable (such as for charge generation, triplet formation, and OLED applications), as well as for applications where the non-radiative decay process itself is desirable.

We suggest that the intermolecular hydrogen bond that is formed in non-substituted diketopyrrolopyrrole derivatives is responsible for the rapid deactivation of the Red 254 excited state. We hypothesise that the mechanism by which this non-radiative decay occurs is by partial proton transfer across the N–H···O hydrogen bond between adjacent molecules, forming a temporary tautomer form of the molecule under excitation. This scheme is illustrated in Fig. 8.

This is supported by the work of Mizuguchi,[35] in which they find that the formation of the hydrogen bond in Red 254 is responsible for the bathochromic shift of the $S_0 \leftrightarrow S_1$ transition overcoming the hypsochromic contribution from the van der Waals interaction, resulting in the overall red-shift to the ground state absorption spectrum, similar to that in Mizuguchi and Wooden.[36]

To verify this hypothesis, we have performed ultrafast time-resolved infra-red spectroscopy and density functional energy calculations in order to find which bond vibrations are involved in the non-radiative decay process of Red 254. We anticipate that the effect of intermolecular hydrogen bonding will be visible in the transient infra-red spectra by a bleaching of the carbonyl bond signal. We expect to see some component of the time-resolved infra-red decay to decay with the same lifetime as the excited state decay of the UV-vis TA signal seen in Fig. 4.

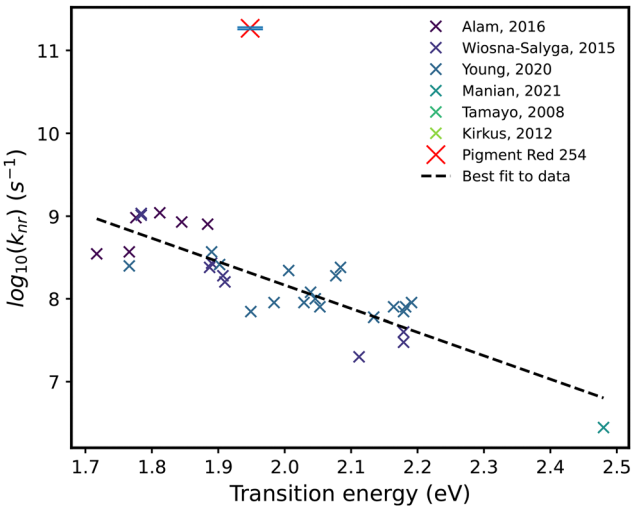

Fig. 7 Comparison of the energy gap law relationship in diketopyrrolopyrrole derivatives, plotting the base-10 logarithm of the nonradiative decay rates of a range of molecules with diketopyrrolopyrrole cores against their transition energy from the excited state to the ground state. This data was collected from Manian *et al.* 2021,[30] Alam *et al.* 2016,[31] Wiosna-Salyga *et al.* 2015,[32] and Young *et al.* 2020.[23] Also marked on this graph is the rate and energy of the non-radiative decay of Red 254, demonstrating that said non-radiative decay takes place over much faster timescales than is typical of molecules of this type, indicating a different mechanism of decay.

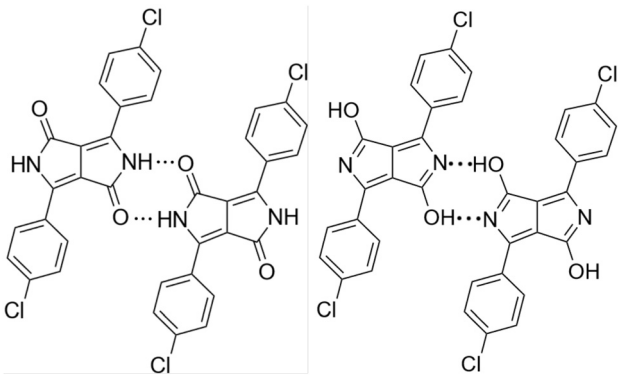

Fig. 8 Proposed structure of intermolecular tautomerisation of Red 254 in the solid state. The left figure shows the un-tautomerised molecule, with the N–H···O interaction highlighted with dotted lines. The right figure shows the proposed form of the tautomerised molecule, in which the hydrogen atom has been transferred to the oxygen, slightly altering the conjugation of the pyrrole core.

The vibrational modes from the density functional theory (DFT) calculations are shown in Fig. 9. The scaling factor used in this plot is that detailed in Merrick *et al.*[37] Four modes were selected by virtue of their IR strength intensity as well as their relevance to modes of interest, specifically phenyl hydrogen wagging modes and stretching modes (Fig. 12(a), 1410 cm^{-1}, purple), a C═O stretching and pyrrole C═C stretching mode (Fig. 12(b), 1684 cm^{-1}, blue) a similar pyrrole C═C stretching combined with internal intermolecular carbonyl stretching mode (Fig. 12(c), 1751 cm^{-1}, teal) and external intermolecular

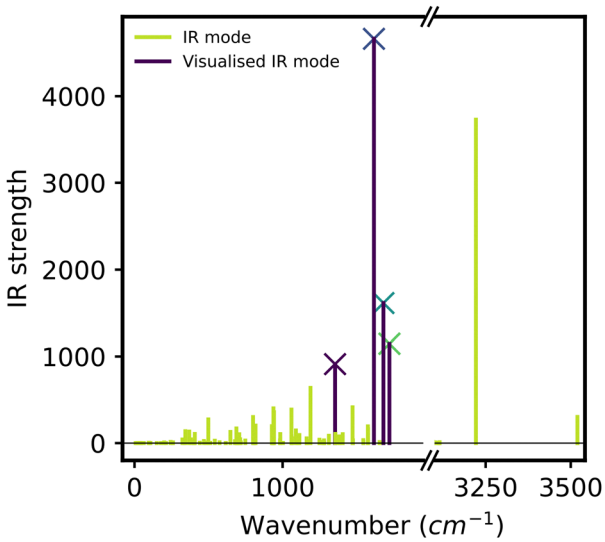

Fig. 9 Spine plot of modes found *via* density functional theory calculations, shown with vertical lines against their predicted infra-red activity strength. Modes which are visualised and shown in Fig. 12 are shown in purple, with colour-coded *X* markers at their maximum value, while those not visualised are shown in green.

carbonyl stretching mode with minimal contribution from the internal pyrrole modes (Fig. 12(d), 1793 cm^{-1}, green).

In addition, the high-energy modes around 3200–3600 cm^{-1} are identified with vibrations involving hydrogen single bonds, such as C–H and N–H bonds. Mizuguchi and Wooden[36] identify this mode in diphenyl-DPP as corresponding to broad N–H IR absorption, suggesting this mode represents stretching of the hydrogen side group bond attached to the nitrogen atom. These mode energies are unlikely to be exact, due to this molecule not being modelled in a crystalline lattice for simplicity, resulting in energetic differences due to a lack of π–π stacked adjacent molecules and the presence of external modes which are not effected by intermolecular interactions.

This is especially evident in the difference in the energy of carbonyl stretching between the modes shown in Fig. 12(c) and (d). However, these are a useful approximation to aid in mode identification, together with previous mode identifications in similar molecules from the literature.

Fig. 10 shows the Fourier transform infra-red (FTIR) spectrum of Red 254 thermally deposited on a calcium fluoride substrate, background corrected with a blank calcium fluoride window. The high energy feature in the FTIR spectrum at ~3000 cm^{-1} is assigned to a broad N–H stretching mode, based on the paper by Soberats *et al.*[38] and on the analysis of the similar molecule by Mizuguchi and Wooden.[36] This assignment corresponds to the high-energy modes around 3200–3600 cm^{-1} in the DFT calculations, showing agreement within ~500 cm^{-1} between experiment and calculation. As this bond's vibrational modes are the most likely to be affected by inclusion of more molecules in simulation due to the N–H bond's importance to the intermolecular interactions in diketopyrrolopyrroles,[35,39] this level of accuracy is sufficient for this assignment. Below 1723 cm^{-1}, the density of peaks

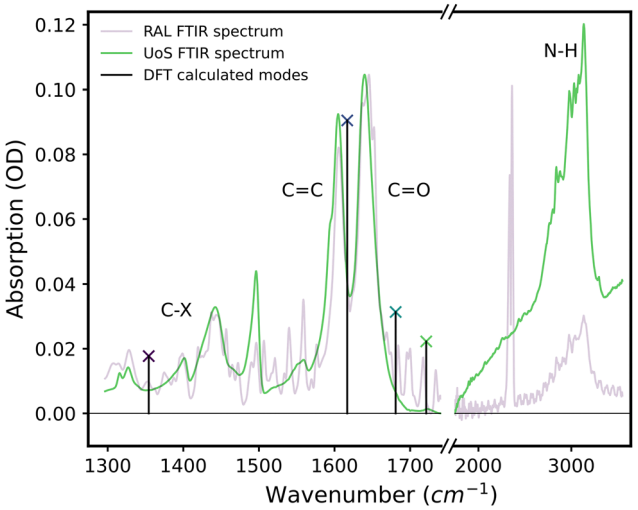

Fig. 10 Fourier transform infra-red (FTIR) spectra of thermally sublimated film of Red 254 on a calcium fluoride substrate. The spectrum in purple was taken using the instrument at the Rutherford Appleton Laboratory. The spectrum in green was taken using the instrument at the University of Sheffield. The FTIR is shown on two different wavenumber scales, as the peaks between ~1350 cm^{-1} and 1723 cm^{-1} are much more tightly spaced than the longer wavenumber spectrum. The modes shown in the vector plot in Fig. 12 are marked on this plot with normalised vertical black lines, and colour coded *X* markers.

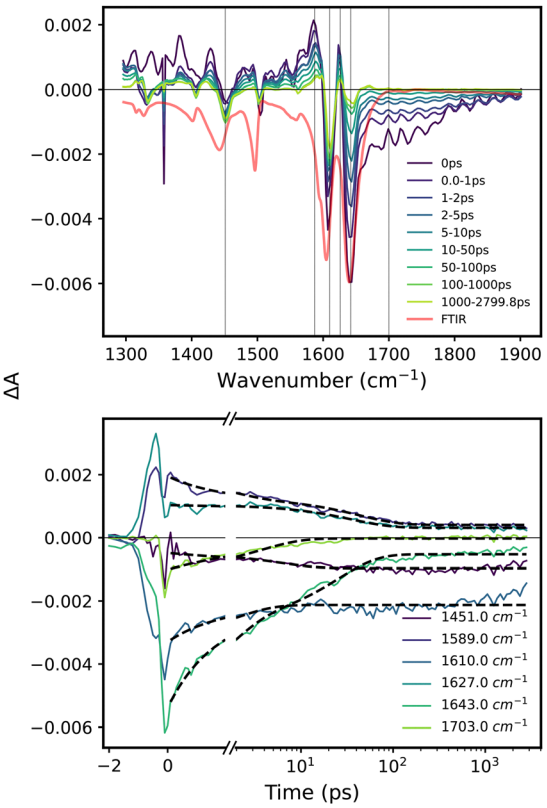

Fig. 11 Time resolved infra-red (TRIR) spectra (top) and kinetics (bottom) of thin film of Red 254 on calcium fluoride window substrate, using a pump wavelength of 520 nm and power of 5 mW. An additional broad electronic signal was seen in all TRIR spectra, and was subtracted from the overall spectrum by subtracting the signal between 2000–2100 cm^{-1}, as the signal appeared the same across the spectrum. The subtracted kinetics are shown in Fig. 13. Overlaid with these spectra is the inverted Fourier transform infra-red (FTIR) obtained from the Rutherford Appleton Laboratory spectrometer, to assist in identifying the peaks. The locations of the kinetic slices used in TRIR kinetics (bottom) are marked by grey lines on the figure. Exponential and bi-exponential fits to the data are shown on this graph as dotted black lines.

increases, and thus is shown in Fig. 10 with a scaled axis. The most prominent peaks in this spectrum are two peaks between ~1600 cm^{-1} and ~1650 cm^{-1}. These bonds occur in a region commonly associated with carbon double-bond stretching modes.[40,41] We specifically assign the lower peak at 1626 cm^{-1} to a C=C stretching mode, and and the higher peak at 1640 cm^{-1} to C=O stretching. We make these identifications partially due to the modes highlighted in the DFT calculations (Fig. 9 and 12), in which the lower energy intense peaks have a large contribution from pyrrole C=C bond stretching, whereas the higher energy modes have large C=O stretching contributions, as well as from assignments made by Mizuguchi and Wooden.[36]

There are many low-intensity peaks present in the FTIR spectrum below 1600 cm^{-1}, and it is difficult to identify each of them individually, especially as the DFT calculations are not exact. However, this region is associated with C–N and C–C stretching modes.[41] From the DFT calculations in Fig. 9 and 12(a), many modes in this region are associated with breathing and stretching modes associated with the phenyl groups, as well as hydrogen wagging modes.

To examine how the molecular vibrations change over time on excitation, time resolved infra-red spectroscopy (TRIR) was performed on the thin film sample, using an excitation wavelength of 520 nm. The resultant spectra and kinetics are shown in Fig. 11 (top) and (bottom) respectively, for a pump power of 5 mW.

The TRIR spectra show two negative bleach signals corresponding to the C=O and C=C stretching mode peaks at 1643 cm^{-1} and at 1610 cm^{-1}, respectively. This assignment is made due to their overlap with the previously assigned modes from the FTIR spectrum, in addition to the previous assignments from the literature.[36,40,41]

These bleach signals overlap with an excited state absorption (ESA) feature, from ~1600 cm^{-1} to ~1650 cm^{-1}. We suggest that this mode corresponds to a C=N stretching mode, as it is in the same region as the other carbon-double-bond mode assignments, and its energy lies between that of the C=O and C=C bond stretching mode energies. This corresponds well with the proposed model of proton transfer, in which the C=O bond has been bleached and a C=N ESA feature has appeared. A broad time dependent signal was observed in the TRIR spectra, and was present across the whole examined region. This signal was assigned to an electronic signal overlaid with the vibrational peaks, and the average of this signal between 2000–2100 cm^{-1} was subtracted from the overall transient infra-red spectra,using the approximation that the broad signal varies only a small amount across the region of interest. The TRIR spectra shown in

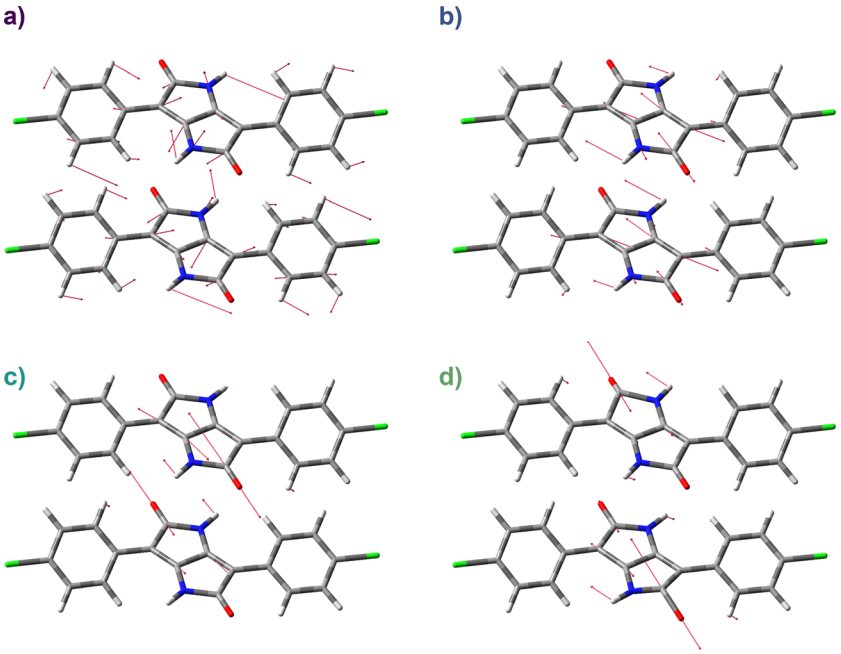

Fig. 12 Vector plots of vibrational modes of Red 254 dimers as found *via* DFT calculations. The modes shown are (a) 1410 cm^{-1}, (b) 1684 cm^{-1}, (c) 1751 cm^{-1} and (d) 1793 cm^{-1}.

this paper are all corrected for the electronic signal in this manner. The subtracted kinetics, for pump powers 0.5 mW, 1 mW, 2.5 mW, and 5 mW, are shown in Fig. 13, and have a lifetime of 11 ± 1.2 ps. At lower energies, there are bleached peaks corresponding to the smaller features which we have previously assigned to miscellaneous phenyl and C–N stretching modes, as well as C–C and ring breathing modes.

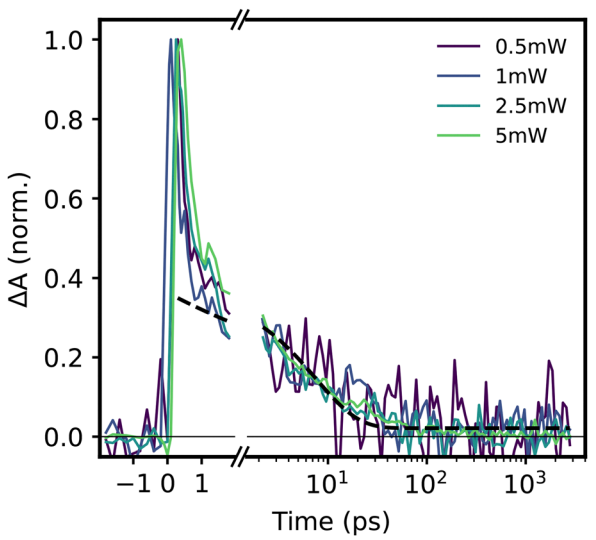

Fig. 13 Normalised kinetic decays of the 2000–2100 cm^{-1} kinetic slice of time-resolved infra-red spectrum of Red 254 evaporated thin film on calcium fluoride substrate, using an excitation wavelength of 520 nm, at fluences 0.5 mW, 1 mW, 2.5 mW, and 5 mW. These decays are fitted with exponential decays after 1 ps, and the average of these lifetimes are displayed as a black dotted line.

Table 3 shows the differences between the calculated and experimentally determined wavenumbers as assigned to each mode: approximate carbon single-bond modes, C═O, C═C, and C═N stretching modes. As the C═N feature only appears as an excited-state feature, and does not appear in the FTIR or DFT spectra, these are not shown for comparison. Two C═N wavelengths are specified due to the broad feature overlapping with the C═C stretching mode in a manner that is difficult to separate. The kinetic decays of the TRIR are shown in the lower figure. At negative times there is a coherent artefact response, and as such the time-zero point is set after the decay of the initial strong signal. The decay of the bleach signals <1600 cm^{-1}, which have been identified with carbon-single-bond modes such as phenyl modes, are separated into two groups: the bleaches at 1383 cm^{-1} and 1426 cm^{-1} decay with the same lifetime as the C═N ESA peak at 1582 cm^{-1}, and similarly to the 1623 cm^{-1} ESA peak, and thus are not represented in the kinetics.

The ESA at the low-energy end of the spectrum at 1334 cm^{-1} as well as the bleach peak at 1504 cm^{-1} decay with the same kinetic shape as the bleach at 1451 cm^{-1}. As the 1451 cm^{-1} peak is the most intense, this decay is plotted on Fig. 11. The broad high energy bleach at 1700 cm^{-1} as well as the C═C and C═O bleach features (at 1610 cm^{-1} and 1643 cm^{-1}) decay on distinct timescales and thus are shown as well.

This is done to group together redundant decays, as well as to identify which modes are related in different excited states. In TRIR spectra, each peak corresponds to a different vibration which may decay on its own timescale, which contrasts with transient absorption spectra in which the signals arise from typically one or two electronic excited states at a time.

Table 3 Table of different wavenumbers (n) assigned to vibrational modes in the DFT calculations, FTIR spectrum, and TRIR spectra. C–X refers to a generic, approximate or representative carbon single-bond mode. "s" denotes a stretching mode, while "w" denotes a waving or bending mode

Bond	DFT ν (cm^{-1})	DTIR ν (cm^{-1})	TRIR ν (cm^{-1})
C–X s/w	~1410	1443	~1451
C═N s (1)	—	—	1589
C═C s	~1684	1605	1610
C═N s (2)	—	—	1627
C═O s	1751/1793	1642	1643

In making these comparisons, we have said that the complex spectrum below ~1600 cm^{-1} represent two different associated sets of vibrations: one which decays at the same rate as the tautomer, evidenced by the C═N ESA features decaying with a similar lifetime, and one which has distinct decay dynamics. In addition, the decay of the C═C and C═O bleaches are distinct, meaning that the C═C bleach feature is not uniquely associated with the proton-transfer induced tautomerisation.

Fits to the kinetic decays are shown on these figures as dotted black lines. The 1451 cm^{-1}, 1610 cm^{-1}, 1627 cm^{-1}, and 1700 cm^{-1} kinetic slices are modeled as exponential decays, whereas for the 1587 cm^{-1} and 1643 cm^{-1} component, it was found to be best modeled with two exponential components, as an approximation to estimate the lifetimes of the decays, similar to the transient absorption data in Fig. 4 and 5. The lifetimes extracted from these plots *via* the fits are shown in Table 4 for the highest pump power plot, at 5 mW.

The decay seen at 1700 cm^{-1} decays with a single lifetime component of 3.7 ± 0.27 ps, and is well described with a monoexponential decay, leaving very little residual signal. This timescale matches well with the excited state decay seen in the transient absorption data, which had a lifetime of ~5 ps (seen in Fig. 5). This further corroborates the assignment of the broad signal to the electronic excited state decay, with this broad decay being a baseline artefact remaining due to the electronic signal being approximated as constant over the wavelength range examined.

The 1451 cm^{-1} kinetic grows with time, which with an exponential model has a time constant for this growth of 5.8 ± 1.26 ps, which is also similar to the lifetime of the electronic excited state decay. This indicates that as the non-radiative decay occurs from the excited state, the resultant thermal artefact enhances some of the low-energy signals in the TRIR spectrum. This may be *via* classical heating artefact which changes the local refractive index of the sample. However, as this artefact is not consistent across this region, with some instead decaying concurrently with the C═N mode, this could be interpreted as population of quantised vibrational energy levels, localised on carbon-single-bond and phenyl modes. Due to the overlap of signals in this region, however, it is difficult to make a definitive statement.

There are four peaks that will be analysed in the carbon double-bond region: an excited-state absorption (ESA) peak at 1582 cm^{-1}, a ground-state bleach (GSB) peak at 1610 cm^{-1}, another ESA peak at 1627 cm^{-1} and a final GSB peak at 1643 cm^{-1}. As described previously, the two ESA peaks represent a single C═N ESA peak overlapped with the lower energy C═C stretching GSB, at 1610 cm^{-1}. The low-wavenumber ESA peak, as well as the two GSB peaks, have an initial short decay lifetime component of 1.7 ps, 1.9 ps and 1.5 ps, for the 1587 cm^{-1} C═N ESA peak, C═C GSB peak, and C═O GSB peak respectively. The 1627 cm^{-1} C═N ESA peak does not have this lifetime, which may be due to its overlap with the C═C counteracting this decay component.

The 1610 cm^{-1} peak, associated with the C═C stretching mode of the diketopyrrolopyrrole core, decays slightly with this lifetime before plateauing, and the final decay of the peak takes place over longer timescales than those that were available for the ULTRA TRIR spectrometer. This indicates that the reduction in IR strength of the C═C mode lasts for a much longer timescale than the electronic excitation, and that this mode plays a significant part in the long-lived thermal artefact that was observed in the TA data.

For the remaining carbon-double-bonded peaks, there is a longer-lived decay component with lifetimes of 43 ps, 36 ps, and 25 ps for the 1589 cm^{-1} and 1627 cm^{-1} C═N ESA as well as the 1643 cm^{-1} C═O GSB kinetics, respectively. As this lifetime is associated with the C═O bleach, this lifetime can be assigned to the decay of the proposed proton-transfer tautomer bond, as the recovery of the un-tautomerised conformer would result in a recovery of the carbonyl bond. This further confirms that the ESA peak overlaid with the C═O and C═C peaks is due to the formation of C═N bonds in the tautomer.

Finally, these three peaks also retain some population at long times, that does not decay over the course of the experiment. This can be explained *via* the same thermal artefact seen in the lower energy region as well as in the UV-vis Red 254 TA (Fig. 4).

The difference between the fitted lifetimes of these peaks can be explained due to the close spacing of the peaks in the <1650 cm^{-1} region, resulting in a difficulty of separating these peaks, as well as potential overlap with any residual excited electronic signal.

TRIR of thin films of Red 254 was performed with a range of pump powers, to investigate the effect of varying fluence on the excited state decay of the molecule. Full spectra and kinetics for pump powers 0.5 mW, 1 mW, and 2.5 mW are shown in ESI,† Fig. S9–S11, and the fitted decay lifetime parameters for these pump powers are summarised in Table S2.

Table 4 Lifetimes of excited vibrational decays from time-resolved infra-red spectroscopy kinetics as shown in Fig. 11. The pump power used for these measurements was 5 mW

Wavenumber (cm^{-1})	τ_1 (ps)	τ_2 (ps)	$\delta\tau_1$ (ps)	$\delta\tau_2$ (ps)
1451 (C single-bond GSB)	5.8	—	1.26	—
1589 (C═N ESA)	1.7	43	0.23	3.6
1610 (C═C GSB)	1.9	—	0.32	—
1627 (C═N ESA)	36	—	2.7	—
1643 (C═O GSB)	1.5	25	0.12	1.8
1703 (electronic)	3.7	—	0.27	—

Each kinetic discussed earlier, at each pump power taken (0.5 mW, 1 mW, 2.5 mW and 5 mw), grouped by wavenumber (1451 cm^{-1}, 1589 cm^{-1}, 1610 cm^{-1}, 1627 cm^{-1}, 1643 cm^{-1}, and 1703 cm^{-1}), are shown in Fig. S12, S13, S14, S15, S16, and S17 (ESI†) respectively. Decay fits of each kinetic were performed in the same manner as for the 5 mW kinetics, and the pump-power dependency of the decay lifetime of each wavenumber are shown in Fig. S18, S19, S20, S21, S22, and S23 (ESI†) respectively.

3 Discussion

While the modelling proposed above is imprecise, it demonstrates that there are ~3 separate decay lifetimes that are visible: there is a very rapid, 1–2 ps timescale decay, that is visible in the 1589 cm^{-1}, 1610 cm^{-1} and 1643 cm^{-1} kinetic traces, all of which we have identified with carbon-double-bond features: C═N, C═C, and C═O. There is also a 3.5–5 ps lifetime that we have compared to the ESA decay lifetime in the TA, that is visible in the 1451 cm^{-1} kinetic trace as a growth feature, as well as in the the 1703 cm^{-1} kinetic trace which is associated with the electronic excited state. Finally, there is a >10 ps lifetime, which is present in the carbon-double-bond features: 1589 cm^{-1}, 1610 cm^{-1}, 1627 cm^{-1} and 1643 cm^{-1}. In addition, there is signal in the TRIR that lasts beyond the range of the experiment, primarily shown in the 1610 cm^{-1} and 1451 cm^{-1} decays.

Proton transfer has been observed to facilitate non-radiative decay in a number of molecular systems similar to that of Red 254. It is well known to occur between DNA nucleobases, which functions as a photoprotection mechanism to avoid solar damage to organism's vulnerable genes.[43,44] Non-radiative decay due to hydrogen-bond induced proton transfer has been observed in fluorenone derivatives in alcoholic solutions.[45–47] In this environment, there is strong hydrogen bonding between the fluorenone and solvent that strengthens in the excited state, reducing the excited state energy and enhancing vibronic relaxation,[45,46] over timescales that can be as short as femtoseconds.[47] This demonstrates that this mechanism can operate over the ultra-short timescales observed for the non-radiative decay in Red 254.

We propose a model for these observations based on this intermolecular proton transfer mechanism, taking into consideration the observed lifetimes in the previously examined transient absorption spectra:

(1) Initial excitation and tautomer formation: due to the lack of growth of the tautomer-associated signals (the C═N identified ESA at 1589 cm^{-1} and 1627 cm^{-1}), we suggest that hydrogen-bond induced proton transfer happens very rapidly, with a timescale sufficiently short to be obscured by short-time artefacts and chirp correction.[48] Due to the extremely rapid timescale of the tautomer formation, occurring on a timescale <1 ps, we consider that the excited state itself has partial tautomer character; a change in the charge density on the diketopyrrolopyrrole core in the excited state results in the broad, red-shifted excited state potential energy surface that allows the molecule to tautomerise *via* vibrational relaxation. This can be considered qualitatively as the hydrogen nucleus becoming more mobile in the excited state, and being attracted to the oxygen site on the adjacent molecule.

(2) Vibrational relaxation: after excitation, the partially-tautomer S_1 state is prepared in a non-equilibrium vibrational state. As Kasha's rule states that vibrational decay happens over ~ps timescales, we assign the 1–2 ps decay lifetime of the carbon-double-bond features around 1580 cm^{-1}–1650 cm^{-1} to vibrational decay to the excited state potential energy surface minimum.

(3) Conical intersection with charge transfer state: we know that the excited state that is observed in the TA is lost over a ~5 ps timescale. As such, we identify the following 3.5–5 ps timescale decay observed in the TRIR with a non-avoided conical intersection with a dark charge transfer state which permits rapid non-radiative relaxation to the ground state, which itself has tautomer character. The picosecond scale lifetime of this decay suggests a small energy barrier to the decay at this intersection. We identify this state as a dark charge transfer state rather than a non-bonding $n\pi^*$ orbital due to the presence of the near-IR electronic signal that has been previously discussed. This broad near-IR absorption is typical of molecular polaronic states.

In addition, the presence of charge transfer states has previously been used to explain the broad red-shifted steady state absorption spectrum.[34,35,46] The presence of the charge transfer state broadens the S_1 potential energy surface *via* resonant interactions. The high rate of this conical intersection mediated non-radiative decay is responsible for the negligible emissivity of Red 254 in the solid state. That it decays to a tautomer state is demonstrated by the persistence of the C═N feature, and we know that this decay is significant as the ESA visible in the UV-vis TA (Fig. 4) disappears along this timescale, the electronic state at 1703 cm^{-1} disappears on this timescale, and the phenyl associated single carbon bonds below ~1600 cm^{-1} increase in intensity on this timescale.

(4) De-tautomerisation: after decaying to the tautomer ground state local minimum, the original form of the molecule is recovered over an approximate 10–50 ps timescale, as the ESA peaks associated with the C═N bond, as well as the C═O bleach, decay on this timescale, indicating the re-formation of the N–H and C═O bonds. This longer timescale governing the loss of the C═N bond is what suggests that the tautomerised conformer is not stable, and the un-tautomerised ground state minimum is a lower energy configuration.

(5) Thermal relaxation: the residual signal present beyond the timeframe accessible by the ULTRA TRIR spectrometer is likely due to the same thermal artefact seen in the UV-vis TA spectrum at late times, that is a classical heating artefact arising from the excess vibrational energy.

This model is illustrated by the schematic in Fig. 14, and is similar to that proposed by Kurihara *et al.*[49] in their investigation of photoinduced intramolecular hydrogen transfer in 2-[2-(2-pyrrolyl)ethenyl]pyridine, save for the addition of a

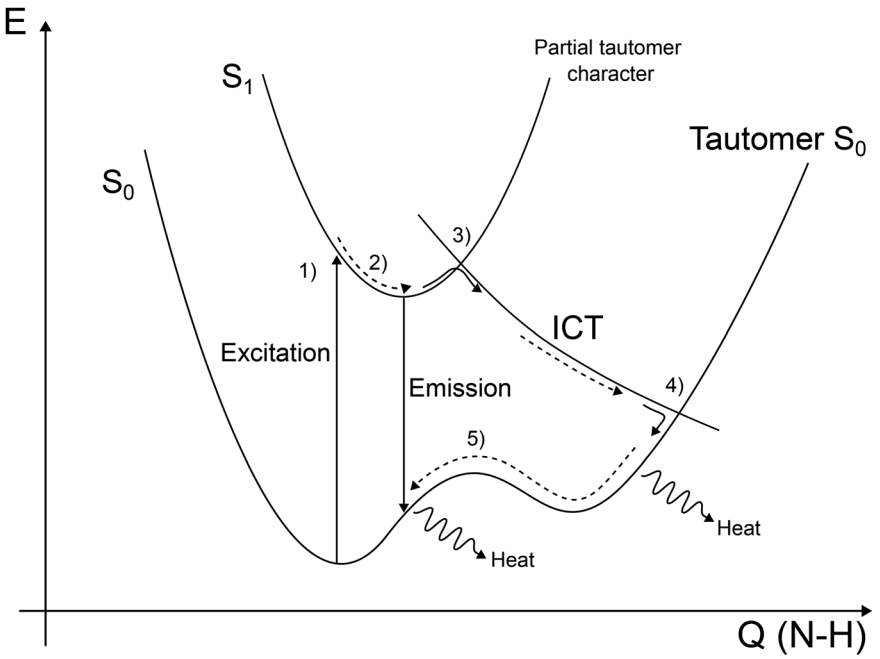

Fig. 14 Model of the non-radiative decay of Red 254, following the model detailed in this section. Shown on axes of energy *E vs.* molecular normal coordinate *Q*, which has some character mediating the N–H inter-nuclear distance. Step (1) excitation of the molecule into the excited S_1 state, which has partial tautomer character due to changes in charge density on the diketopyrrolopyrrole core. Step (2) 1–2 ps timescale of vibrational relaxation according to Kasha's rule.[42] Step (3) conical intersection with an intermolecular charge transfer state, resulting in rapid ~5 ps timescale relaxation to the ground state in step (4), which still maintains tautomer character. This charge transfer state results in the hydrogen atom being driven to form a semi-stable tautomer. Step (5) the tautomer is unstable, resulting in a relatively slow recovery of the un-tautomerised ground state. The excess energy in this and the previous step are lost to the environment as heat.

non-avoided crossing, or conical intersection, which facilitates the rapid non-radiative decay to the ground state. They show similar shifted emission spectra to those seen in Fig. 2 in the solid state (bottom). However, in this case, fluorescent processes are significantly more impactful to the overall dynamics, which may indicate a potentially different mechanism of non-radiative decay.

In step 3, we do not have direct evidence to say definitively whether a conical intersection occurs, and a conical intersection is not the only possible source of this phenomenon. However, these crossings are known to occur in systems mediated by proton transfers due to changes in the symmetry of the molecule permitting these diabatic crossings. As such, the lifetime of this decay is either determined by a rate-limiting energy barrier in the excited state potential energy surface, or the decay proceeds with a gap law decay *via* a reduced, ~0.9 eV energy gap. This value is based on the trend of the energy-gap-law mediated non-radiative decay from literature shown in Fig. 7, by extrapolating the expected energy value of Red 254 with its 5 ps lifetime on this trend line.

This model is supported by previous research into the charge transfer states of diketopyrroloypyrrole derivatives. Głowacki *et al.*[50] have used DFT calculations to link the strength of the charge transfer character in DPP derivative dyes including Red 254 to the strength of the intermolecular hydrogen bond. They study phenyl-substituted DPP (PhDPP) as well as p-position bromine- and chlorine-substituted DPP, p-Br-PhDPP and p-Cl-PhDPP, the latter molecule being synonymous with Red 254. They demonstrate that while in p-Br-PhDPP and p-Cl-PhDPP the contributions to the charge carrier mobility are lower than in unhalogenated PhDPP, its contribution is at least 12% in all three molecules.

The charge transfer state for which the hydrogen bonding behaviour is a strong mediating force has been used to affect the decay pathways of the excited state in multiple ways. A series of papers by Mauck *et al.* have demonstrated that in a range of phenyl-DPP derivatives, the charge transfer state can be an intermediate state for generating triplet pairs *via* singlet fission. While singlet fission does not occur in Red 254, these papers demonstrate the energetic relaxation which occurs due to excited state conversion to charge transfer states in diketopyrrolopyrroles, which is observed in Red 254's highly Stokes shifted low-yield fluorescence.[14,15,33]

Similar charge transfer state-mediated non-radiative decay has been seen in Liang *et al.*,[51] where a ferrocenyl DPP derivative is used as a dye for cancer-treating photothermal therapy. In this work, a photo-induced electron transfer mechanism is proposed, forming a charge transfer state which quenches singlet and triplet populations to produce heat *via* non-radiative decay, similar to the effect seen in the nanosecond scale transient absorption measurement of Red 254 (see Fig. 5 and 7).

Charge transfer states have also been linked with proton transfer in Red 254 previously. It is noted in Mizuguchi and

Wooden[36] that proton transfer occurs as a possible result of the charge transfer formation changing the electron density on the nitrogen atom of diphenyl-diketopyrrolopyrrole. In addition, Ruiz-Carretero *et al.*[52] identify both the oxygen and nitrogen atoms as being involved in hydrogen bonding behaviour. As such, we confidently assign the intermediate dark state observed in this process as a dark charge transfer state which drives the inter-molecular proton transfer between the nitrogen and oxygen of adjacent molecules.

By the arguments presented in this and the previous section, we have determined that Pigment Red 254 does not undergo singlet fission as predicted by the work of Padula *et al.*,[5] but rather undergoes efficient picosecond-scale non-radiative decay to the ground state *via* proton transfer tautomerisation enabled, likely charge transfer state mediated conical intersection with the ground state, and produces a significant thermal artefact in the long time TA and TRIR spectra that is reproducible *via* sample heating. This highlights the importance of considering more than singlet and triplet energies when predicting a material's viability for singlet fission sensitisation, as the presence of intermolecular hydrogen bonding is known[53–55] to encourage proton transfer and non-radiative decay, which results in a loss mechanism for singlet fission.

However, despite the lack of singlet fission found in Red 254, its rapid, efficient non-radiative decay may prove of interest to the fields of photoprotection, in a mechanism similar to that shown by DNA nucleotides, photothermal therapy such as photo-induced ablation of organic tissue such as cancer cells,[56] if the molecule is found to be safe *in vivo*, or as a building block for a larger, polymerised photothermal therapy sensitiser. In addition, its stability in harsh environmental environments would make it ideally suited for solar-driven water purification.

4 Methods

4.1 Sample preparation

Solid samples were prepared *via* thermal evaporation onto quartz coated glass, sapphire or calcium fluoride substrates (Ossila). Substrates were first cleaned by sonication at 60 °C for 10 minutes in de-ionised water mixed with Helmanex III cleaning concentrate, followed by pure de-ionised water, acetone, and isopropanol. They were then cleaned further with a Bioforce Nanosciences UV-Ozone cleaner for 10 minutes. Deposition was performed using an Angstrom Engineering vacuum deposition kiln with a target thickness of 200 nm at 0.2 Å s^{-1}, using PID control and thickness measured using a quartz microbalance.

Solution samples were prepared by adding 3 ml of dimethyl sulfoxide (DMSO) to 10 mg of Pigment Red 254 in a glass vial. At this time, no solvation was visible. A magnetic stirbar was added to the mixture which was then stirred at 2000 rpm and heated to 195 °C using a hot plate under a ventilated fume hood. The cap was left on (unscrewed) to promote condensation of any vapours that arose. After 15 minutes, the solvent changed to a visibly yellow colour, indicating dissolution. Even so, there was undissolved solute remaining, as Red 254 is very insoluble even in DMSO, and was filtered from the solution using a PTFE syringe filter. This solution was then diluted using DMSO by 100 times for use in transient absorption spectroscopy.

Samples of Red 254 in solid and solution phase are shown in Fig. 1(c). Once the solubility of Red 254 was known, solution samples for concentration dependent emission were prepared by first producing a stock solution, with a concentration of 50 μg ml^{-1}, by adding 800 μg of Red 254 pigment to a glass phial, then covering with 16 ml of DMSO. Sample was then heated, stirred, and filtered as described above. Samples for steady-state spectroscopy were prepared by diluting the stock sample by 10 times (5 μg ml^{-1}), 100 times (500 ng ml^{-1}) and 1000 times (50 ng ml^{-1}) in order to test the concentration dependence of the sample emission.

Steady state emission spectra were taken as described below with samples prepared in 1 mm cuvettes (for the 50 μg ml^{-1} and 5 μg ml^{-1} samples) and 10 mm cuvettes (for the 500 ng ml^{-1} and 50 ng ml^{-1} samples). These spectra are shown in Fig. S1 (ESI†).

4.2 Steady-state spectroscopy

Absorption and emission measurements of thin film samples were taken using an Ocean Insight Flame fiber coupled mini spectrometer. For the absorption spectrum, the light source used was a Halogen-Deuterium Ocean Insight DH 200 BAL lamp.

The absorption spectrum was inferred based on the percentage transmission of the lamp's light through the sample. The light source used for emission measurements was a 405 nm CW semiconductor diode laser with laser power 2.85 mW.

Absorption and emission measurements of Pigment Red 254 in solution of DMSO were performed using a Horiba Fluoromax 4 spectrofluorometer. The sample concentration used was 500 ng ml^{-1} to minimise self-absorption effects.

Concentration dependent emission spectra were taken using the same CW laser setup as used for the thin film steady state emission measurement.

For each measurement, background was subtraction was performed using the transmission spectrum of a blank sample, either of a cuvette of equivalent thickness of DMSO or using a blank substrate.

4.3 Picosecond transient absorption spectroscopy

Picosecond transient absorption spectroscopy was performed using an Ultrafast Systems Helios transient absorption spectrometer, described in detail elsewhere.[57] The probe beam was generated using the output from an amplified 10 kHz Ti:sapphire laser (Spectra Physics) at 800 nm to pump a calcium fluoride plate that produced a supercontinuum white light beam. The pump laser used was a light conversion TOPAS prime 10 kHz laser, set to a pump wavelength of 532 nm, driven by the output of the same Spectra Physics laser. The pump beam was triggered at 5 kHz, half that of the probe laser. The data was acquired at pump powers between 0.5–1 mW and pump diameters on the order of 700–1200 μm (probe spot

100–400 μm diameter). We observed no measurable fluence dependence.

Bad point removal, chirp correction, and background subtraction was performed using the Surface Xplorer tool from Ultrafast Systems.

4.4 Nanosecond transient absorption spectroscopy

Nanosecond transient absorption spectroscopy is performed using the output from a 1 kHz 90 fs Spectra Physics Solstice ultrafast amplifier at 800 nm to pump a sapphire plate, generating a broadband white light spectrum from ~450–700 nm. Residual fundamental is filtered out with a shortpass filter. This white light supercontinuum is split with a 50/50 beamsplitter and used as a probe and reference beam for the transient absorption measurement. For a pump we used the second harmonic (532 nm) of an 800 ps Q-switched Nd:YVO4 Innolas Piccolo laser, externally triggered at 500 Hz. Pump, probe, and reference are all focused onto the sample, and the pump and probe are overlapped with one another. The reference beam is focused ~1 cm from the pump and probe, to prevent the reference beam from detecting any pumped species. After exciting the sample, the pump is filtered out using a 532 nm notch filter. The magic angle of polarisation between the two beams are set using a 1/2 wave plate and Glann-Taylor prism. After focusing onto the sample, the transmitted probe and reference beams are made incident onto a Wasatch volume phase holographic grating and made incident on two Hamamatsu S7030 silicon 1D CCDs.

The resultant spectrum is calibrated using a filter wheel with 10 nm bandpass filters at 500, 600 and 700 nm. Acquisition is triggered at 1 kHz electronically using a Stanford DG645 digital delay generator, with data acquisition being triggered by a Entwicklungsbuero Stresing custom built data acquisition board. Triggering, data acquisition and preview, temporal overlap and device connection were all managed by home-built software. Solution data was acquired with a higher pump power than solid samples due to less concern of damage to the sample, at 2 mW. The data was acquired at pump powers between 0.4–0.8 mW and we observed no measurable fluence dependence at long time, as before.

All data acquired through nanosecond transient absorption was treated with background removal using an average of points from before time zero.

4.5 Temperature dependent absorption

Temperature dependent absorption of solid state thin films of Red 254 on sapphire and quartz-coated glass were performed by attaching each sample to a brass flow-through sample holder connected to a water immersion heater. The room-temperature absorption spectrum was acquired using a Cary50-Bio spectrofluorometer at high sensitivity acquisition settings, with an average time of 10 s, a spectral resolution of 5 nm, a scan rate of 30 nm min^{-1}, and a wavelength range of 400–680 nm. The temperature of the water bath was then incremented by 5 °C, and the temperature on the back face of the sample measured using a mercury thermometer. Hot absorption spectra were measured using the same settings and subtracted from the room temperature spectrum to give temperature dependent difference spectra. Steady state absorption measurements were treated as described above.

4.6 Resonance Raman scattering

For free-space ultra-low frequency Raman spectroscopy, the sample is placed on a motorized xyz stage (STANDA-8MTF). The sample is excited using a 532 nm single mode solid state diode pumped laser (Cobolt, 04-01) with a 10 cm^{-1} Bragg notch filters (OptiGrate, BragGrate) used to filter the excitation beam. The beam is then focused onto the sample using a 50× objective (M Plan Apo 50×, Mitutoyo), with numerical aperture = 0.55, providing a spatial resolution of ≈1 μm. Laser power at the sample is typically 0.5 mW (power density ≈ 6.34×10^{-1} W cm^{-1}).

Emission is collected by the same objective. The laser line is attenuated with further 10 cm^{-1} Bragg notch filters and is then coupled to a spectrometer (Princeton Instruments, SP2750) equipped with a high-sensitivity liquid nitrogen cooled charge-coupled device (Princeton Instruments, PyLoN). A 1800 g mm^{-1} grating used provides a spectral resolution of ≈0.4 cm^{-1}. Polarisation optics in both excitation and collection beam paths allow the measurement of co-linear and cross-linear polarisations.

4.7 Quantum chemical calculations

Quantum chemistry calculations have been done with the Gaussian16 suite of programs.[58] The molecular geometry used in these energetic calculations followed the structure found *via* X-Ray powder diffraction methods by Ivashevskaya[20] IR spectra were obtained from the calculated DFT intensities and the vibrational wavenumbers uniformly scaled by 0.96.[59] Every band was represented by a Gaussian function of 10 cm^{-1} half-height width.

Quantum chemical calculations were performed by Dr Samara Medina Rivero of the University of Sheffield, with assistance from Daniel Hook.

4.8 Fourier transform infra-red spectroscopy

Fourier transform infrared spectroscopy (FTIR) is a method of measuring the change in a broad infrared spectrum of light as it passes through a material, and is analogous to UV-vis spectroscopy in that it can measure the light absorption of a sample. While very few atoms or molecules have low enough energy transitions to absorb the infrared light electronically, the vibrational modes of a molecule can be IR active and absorb light. This can be used to probe the chemical structure of a molecule by measuring typical bond absorption.

FTIR is performed with the use of a Michelson interferometer,[60] an optical setup which consists of a beamsplitter to generate two paths or arms of the interferometer, each with a retro-reflecting mirror. One of these mirrors is mobile and can be moved back and forth in the directions of propagation of the laser, and one is fixed. These beams are then recombined at the beamsplitter and made incident on a detector.

An interferogram is formed by translating the movable mirror, as the differences in phase of the light at different

mirror positions and optical path lengths will result in constructive and destructive interference between the beams from the different arms of the interferometer. Different wavelengths of light will have different phase differences at different path length differences which will result in a complex interferogram comprised of many different frequency components. This interferogram can be processed to find the spectrum of the beam of light in reciprocal space using a Fourier transformation, which will give the spectrum of the light intensity as a function of wavenumber (cm^{-1}), the typical format for an infrared spectrum.

Apart from the use of the interferometer and the Fourier transform, this experiment can be run in the same manner as an absorption spectrometer, by measuring the difference in the IR spectrum with and without the thin sample in place. In this manner, an infrared absorption spectrum can be obtained. Fourier transform infra-red spectroscopy (FTIR) on thin film samples of Pigment Red 254 on calcium fluoride substrates was performed using a Nicolet iS10 FTIR spectrometer purged with nitrogen to prevent infra-red absorption from water vapour. Data from a blank substrate measurement of calcium fluoride was subtracted to remove background.

4.9 Time resolved infra-red spectroscopy

Time resolved infra-red (TRIR) spectroscopy of Pigment Red 254 was taken using the ULTRA spectrometer at the Rutherford Appleton Laboratory. The pump and probe beams are generated using a Femtolaser oscillator with a 20 fs pulse length and 50 nm bandwidth, which feeds a Thales Laser Ti-Sapph chirped pulse amplifier. The output of this amplifier which was used gives 10 kHz frequency pulses with a 40–80 fs pulse at 0.8 mJ pulse energy, at a wavelength of 800 nm. These laser pulses are shaped by a telescope system to 0.6 cm, and sent through a compressor which can select pulse lengths of 1–3 ps.

The pump and probe beams are generated separately using the light conversion system, consisting of a set of optical parametric amplifiers (OPAs) which allows the selection of a pump wavelength between 200–20 000 nm with a pulse energy of 0.4 mJ. The pump wavelength used for these experiments was at 520 nm, and the power was adjusted to 0.5, 1, 2.5, and 5 mW for pump power dependent measurements. A 10 μJ portion of the Thales amplifier output is used to generate a broad infrared white light spectrum within this same region. The light range used in these measurements were 1300–1900 cm^{-1}.

The triggering between the two beams were adjusted by modulating the repetition rate of the pump from 10 kHz to 5 kHz, using a TTi C-995 phase chopper. The delay between the two beams are set using multiple Newport IMS600LM delay stages, to physically induce delay. The detection system used is a pair of 256 pixel InGaAs detectors which are aligned in post-processing to probe a broad range of the infra-red spectrum. Further details of the setup and other uses of the ULTRA spectrometer are given in Greetham *et al.*[61]

Chirp correction was performed using data processing algorithm in the provided data processing python class. Background subtraction was performed by subtracting the mean signal pre-time zero.

4.10 Atomic force microscopy (AFM)

Atomic force microscopy (AFM) was taken using a dimension 3100 (Veeco) microscope, equipped with a Nanoscope 3A feedback controller and a Scout 350 RAl (NuNano) cantilever. The resonant frequency of this cantilever was 350 kHz and its spring constant was 42 N m^{-1}. The data was processed using Gwyddion Version 2.60,[62] by aligning rows in the software *via* the median method, leveling the data *via* mean plane subtraction, correcting for horizontal scars and applying a zero correction. RMS roughness values were extracted using the 1D method used in the Gwyddion software extrapolated to 2D, using the equation

$$R_{\mathrm{RMS}} = \sqrt{\frac{1}{N}\sum_{ij}^{N} r_{ij}} \tag{2}$$

where N is the number of image pixels and r_{ij} is the height of the image at index ij. The resultant AFM image is shown in Fig. 1(b).

4.11 Further data processing

Franck–Condon fitting of steady state spectra of Red 254 was accomplished using a Franck–Condon fitting python module by David Bossanyi.[22] Franck–Condon fitting was performed using effective vibrational modes extracted from the resonance Raman scattering spectrum in Fig. S2 (ESI†) (top-right) using the following weighted sum equation from Köhler and Bässler[21] for the effective Franck–Condon vibrational mode,

$$E_{\mathrm{eff}}^{\mathrm{vib}} = \sum_i E_i^{\mathrm{vib}} \sigma_i^{\mathrm{Raman}} \Big/ \sum_i \sigma_i^{\mathrm{Raman}} \tag{3}$$

where E_i^{vib} is the vibrational energy of a particular resonance Raman mode i, and $\sigma_i^{\mathrm{Raman}}$ is the resonance Raman intensity of this ith mode. Visualisation of molecular crystal structure of Red 254 was accomplished using the open source Vesta 3D molecular plotting software.[63] The 2D chemical structure of Red 254 was displayed using the PerkinElmer ChemDraw chemical drawing tool.

Conclusions

In conclusion, we have found evidence for non- radiative decay in thin films of Red 254, *via* tautomerisation due to hydrogen-bond mediated proton transfer over a ~5 ps timescale. We have proposed a model for this non-radiative decay involving a proton-transfer induced conical intersection with the ground state which results in long-lived artefact signals in the nanosecond TA and TRIR spectra due to dispersal of the excited state energy as heat. We suggest based on related research on Red 254 and similar molecules that the intermediate state that causes the conical intersection is a dark charge transfer state, which also gives rise to the electronic signal seen in the TRIR

spectra as well as the broad, shifted steady state emission and absorption spectra.

Author contributions

We would like to acknowledge the work done by Dr Samara Medina Rivero, being responsible for the DFT calculations used to find the vibrational modes of the molecule in this work. Furthermore we would like to acknowledge Daniel J. Gillard for acquiring the resonance Raman scattering data used to further evidence claims made concerning the location of vibrational modes and for modes used in Franck–Condon analysis. Finally we would like to acknowledge Rachel Kilbride for acquiring the atomic force microscopy images as well as for assisting in their processing.

Conflicts of interest

There are no conflicts to declare.

Data availability

Data for this article, including steady state UV-vis spectroscopy, transient absorption spectroscopy, time resolved infra red spectroscopy, temperature dependent absorption, Fourier transform infra-red spectroscopy, resonance Raman spectroscopy, AFM and DFT calculations are available at **https://osf.io/axg2b/?view_only=d2de7310133e4d2a9eb4e5d631ba3373**. Furthermore, python code for basic data processing is also provided for transparency of methods used.

Acknowledgements

DH acknowledges support through Engineering and Physical Sciences Research Council (EPSRC) under grant EP/R/513313/1 and the use of the Lord Porter Laser Facility EP/L022613/1 and EP/R042802/1. JC and RKV acknowledge EP/T012455/1, EP/S002103/1. DJG and AIT acknowledge support from EPSRC grants EP/S030751/1, EP/V006975/1, EP/V026496/1, and EP/V007696/1. RK acknowledges support from EPSRC for AFM measurements *via* grant EP/V055127/1 (Manufacturing Organic–Inorganic Nanoparticle Composites with Nanoscale Precision *via* Directed Self-Assembly). We would like to acknowledge the work of Padula *et al.*[5] without whom this work would not have been possible.

Notes and references

1 D. N. Congreve, J. Lee, N. J. Thompson, E. Hontz, S. R. Yost, P. D. Reusswig, M. E. Bahlke, S. Reineke, T. V. Voorhis and M. A. Baldo, *Science*, 2013, **340**, 334–337.
2 A. Rao and R. H. Friend, *Nat. Rev. Mater.*, 2017, **2**, 17063.
3 S. Rühle, *Sol. Energy*, 2016, **130**, 139–147.
4 T. Ullrich, D. Munz and D. M. Guldi, *Chem. Soc. Rev.*, 2021, **50**, 3485–3518.
5 D. Padula, O. H. Omar, T. Nematiaram and A. Troisi, *Energy Environ. Sci.*, 2019, **12**, 2412–2416.
6 E. Švara Fabjan, M. Otoničar, M. Gaberšček and A. S. Škapin, *Dyes Pigm.*, 2016, **127**, 100–109.
7 M. Anghelone, V. Stoytschew, D. Jembrih-Simbürger and M. Schreiner, *Microchem. J.*, 2018, **139**, 155–163.
8 H. Lee, J. Kim, J. Yoo, J. Bae, C. Yoon and J. Choi, *Bull. Korean Chem. Soc.*, 2014, 659–662.
9 S.-H. Choi, O.-T. Kwon, N.-R. Kim, C. Yoon, J.-P. Kim and J.-H. Choi, *Bull. Korean Chem. Soc.*, 2010, **31**, 1073–1076.
10 T.-H. Kim, B.-J. Lee, S.-O. An, J.-H. Lee and J.-H. Choi, *Dyes Pigm.*, 2020, **174**, 108053.
11 W. Kitisriworaphan, T. Chawanpunyawat, T. Manyum, P. Chasing, S. Namuangruk, T. Sudyoadsuk and V. Promarak, *RSC Adv.*, 2021, **11**, 12710–12719.
12 H. Y. Lee, J.-S. Yoo, H.-S. Kwon, J.-K. Oh and J.-H. Choi, *Mol. Cryst. Liq. Cryst.*, 2015, **617**, 73–81.
13 A. Honda, Y. Tamaki and K. Miyamura, *Bull. Chem. Soc. Jpn.*, 2015, **88**, 969–975.
14 P. E. Hartnett, E. A. Margulies, C. M. Mauck, S. A. Miller, Y. Wu, Y.-L. Wu, T. J. Marks and M. R. Wasielewski, *J. Phys. Chem. B*, 2016, **120**, 1357–1366.
15 C. M. Mauck, P. E. Hartnett, E. A. Margulies, L. Ma, C. E. Miller, G. C. Schatz, T. J. Marks and M. R. Wasielewski, *J. Am. Chem. Soc.*, 2016, **138**, 11749–11761.
16 C. E. Miller, M. R. Wasielewski and G. C. Schatz, *J. Phys. Chem. C*, 2017, **121**, 10345–10350.
17 Z. Hao and A. Iqbal, *Chem. Soc. Rev.*, 1997, **26**, 203–213.
18 Z.-Q. Wen, Y.-Q. Feng, X.-G. Li, Y. Bai, X.-X. Li, J. An and M. Lu, *Dyes Pigm.*, 2012, **92**, 554–562.
19 J. Y. Woo, M.-H. Park, S.-H. Jeong, Y.-H. Kim, B. Kim, T.-W. Lee and T.-H. Han, *Adv. Mater.*, 2023, **35**, 2207454.
20 S. N. Ivashevskaya, *Acta Crystallogr., Sect. E:Crystallogr. Commun.*, 2017, **73**, 507–510.
21 A. Köhler and H. Bässler, *The Electronic Structure of Organic Semiconductors*, John Wiley & Sons, Ltd, 2015, ch. 1, pp. 1–86.
22 D. Bossanyi, *franckcondon*, 2020, **https://github.com/fast-spectroscopy-sheffield/franckcondon**.
23 D. C. Young, M. Tasior, A. D. Laurent, L. Dobrzycki, M. K. Cyrański, N. Tkachenko, D. Jacquemin and D. T. Gryko, *J. Mater. Chem. C*, 2020, **8**, 7708–7717.
24 J. Mizuguchi, A. Grubenmann and G. Rihs, *Acta Crystallogr., Sect. B:Struct. Sci.*, 1993, **49**, 1056–1060.
25 V. Ravi Kumar, F. Ariese and S. Umapathy, *J. Chem. Phys.*, 2016, **144**, 114301.
26 S. Albert-Seifried and R. H. Friend, *Appl. Phys. Lett.*, 2011, **98**, 223304.
27 A. Rao, M. W. B. Wilson, S. Albert-Seifried, R. Di Pietro and R. H. Friend, *Phys. Rev. B:Condens. Matter Mater. Phys.*, 2011, **84**, 195411.
28 G. Kim, D. Kim, S. Kang, J. Yoo and H. Kim, *Appl. Sci.*, 2021, **11**, 1535.
29 R. Englman and J. Jortner, *Mol. Phys.*, 1970, **18**, 145–164.
30 A. Manian, R. A. Shaw, I. Lyskov, W. Wong and S. P. Russo, *J. Chem. Phys.*, 2021, **155**(5), 054108.

31 Md. M. Alam, F. Bolze, C. Daniel, L. Flamigni, C. Gourlaouen, V. Heitz, S. Jenni, J. Schmitt, A. Sour and B. Ventura, *Phys. Chem. Chem. Phys.*, 2016, **31**, 21954–21965.
32 G. Wiosna-Salyga, M. Gora, M. Zagorska, P. Toman, B. Luszczynska, J. Pfleger, I. Glowacki, J. Ulanski, J. Mieczkowski and A. Pron, *RSC Adv.*, 2015, **5**, 59616–59629.
33 C. M. Mauck, Y. J. Bae, M. Chen, N. Powers-Riggs, Y.-L. Wu and M. R. Wasielewski, *ChemPhotoChem*, 2018, **2**, 223–233.
34 Y. Qu, J. Hua and H. Tian, *Org. Lett.*, 2010, **12**, 3320–3323.
35 J. Mizuguchi, *J. Phys. Chem. A*, 2000, **104**, 1817–1821.
36 J. Mizuguchi and G. Wooden, *Ber. Bunsen-Ges. Phys. Chem.*, 1991, **95**, 1264–1274.
37 J. P. Merrick, D. Moran and L. Radom, *J. Phys. Chem. A*, 2007, **111**, 11683–11700.
38 B. Soberats, M. Hecht and F. Würthner, *Angew. Chem., Int. Ed.*, 2017, **56**, 10771–10774.
39 Y. Suna, J. Nishida, Y. Fujisaki and Y. Yamashita, *Org. Lett.*, 2012, **14**, 3356–3359.
40 L. Yang, Y. Yu, Y. Gong, J. Li, F. Ge, L. Jiang, F. Gao and Y. Dan, *Polym. Chem.*, 2015, **6**, 7005–7014.
41 N. T. T. Truong, L. T. Nguyen, H. L. T. Mai, B. K. Doan, D. H. Tran, K. T. Truong, V. Q. Nguyen, L.-T. T. Nguyen, M. H. Hoang, T. V. Pham, V. M. Nguyen, T. M. Huynh, T. C. D. Doan and H. T. Nguyen, *J. Polym. Res.*, 2020, **27**, 223.
42 M. Kasha, *Discuss. Faraday Soc.*, 1950, **9**, 14–19.
43 S. D. Camillis, J. Miles, G. Alexander, O. Ghafur, I. D. Williams, D. Townsend and J. B. Greenwood, *Phys. Chem. Chem. Phys.*, 2015, **17**, 23643–23650.
44 Y. Zhang, K. de La Harpe, A. A. Beckstead, R. Improta and B. Kohler, *J. Am. Chem. Soc.*, 2015, **137**, 7059–7062.
45 G.-J. Zhao and K.-L. Han, *J. Phys. Chem. A*, 2009, **113**, 14329–14335.
46 L. Biczók, T. Bérces and H. Inoue, *J. Phys. Chem. A*, 1999, **103**, 3837–3842.
47 G.-J. Zhao and K.-L. Han, *Acc. Chem. Res.*, 2011, **45**, 404–413.
48 M.-H. Kao, R. K. Venkatraman, M. Sneha, M. Wilton and A. J. Orr-Ewing, *J. Phys. Chem. A*, 2021, **125**, 636–645.
49 S. Kurihara, Y. Nishimura and T. Arai, *Bull. Chem. Soc. Jpn.*, 2015, **88**, 963–965.
50 E. D. Głowacki, H. Coskun, M. A. Blood-Forsythe, U. Monkowius, L. Leonat, M. Grzybowski, D. Gryko, M. S. White, A. Aspuru-Guzik and N. S. Sariciftci, *Org. Electron.*, 2014, **15**, 3521–3528.
51 P. Liang, Q. Tang, Y. Cai, G. Liu, W. Si, J. Shao, W. Huang, Q. Zhang and X. Dong, *Chem. Sci.*, 2017, **8**, 7457–7463.
52 A. Ruiz-Carretero, N. R. Ávila Rovelo, S. Militzer and P. J. Mésini, *J. Mater. Chem. A*, 2019, **7**, 23451–23475.
53 H. Zhang, Z. Li, J. Liu and Y. Wang, *J. Mol. Liq.*, 2022, **361**, 119555.
54 P. Zhou and K. Han, *Acc. Chem. Res.*, 2018, **51**, 1681–1690.
55 T. M. Alligrant and J. C. Alvarez, *J. Phys. Chem. C*, 2011, **115**, 10797–10805.
56 W. Hu, X. Miao, H. Tao, A. Baev, C. Ren, Q. Fan, T. He, W. Huang and P. N. Prasad, *ACS Nano*, 2019, **13**, 12006–12014.
57 S. P. O'Connor, S. M. Powell, J. M. Rickman, N. J. Pope, G. D. Noojin, M. O. Scully, M. L. Denton and V. V. Yakovlev, *J. Photochem. Photobiol., B*, 2021, **222**, 112271.
58 M. J. Frisch, G. W. Trucks, H. B. Schlegel, G. E. Scuseria, M. A. Robb, J. R. Cheeseman, G. Scalmani, V. Barone, G. A. Petersson, H. Nakatsuji, X. Li, M. Caricato, A. V. Marenich, J. Bloino, B. G. Janesko, R. Gomperts, B. Mennucci, H. P. Hratchian, J. V. Ortiz, A. F. Izmaylov, J. L. Sonnenberg, D. Williams-Young, F. Ding, F. Lipparini, F. Egidi, J. Goings, B. Peng, A. Petrone, T. Henderson, D. Ranasinghe, V. G. Zakrzewski, J. Gao, N. Rega, G. Zheng, W. Liang, M. Hada, M. Ehara, K. Toyota, R. Fukuda, J. Hasegawa, M. Ishida, T. Nakajima, Y. Honda, O. Kitao, H. Nakai, T. Vreven, K. Throssell, J. A. Montgomery, Jr., J. E. Peralta, F. Ogliaro, M. J. Bearpark, J. J. Heyd, E. N. Brothers, K. N. Kudin, V. N. Staroverov, T. A. Keith, R. Kobayashi, J. Normand, K. Raghavachari, A. P. Rendell, J. C. Burant, S. S. Iyengar, J. Tomasi, M. Cossi, J. M. Millam, M. Klene, C. Adamo, R. Cammi, J. W. Ochterski, R. L. Martin, K. Morokuma, O. Farkas, J. B. Foresman and D. J. Fox, *Gaussian ~ 16 Revision C.01*, Gaussian Inc., Wallingford CT, 2016.
59 A. P. Scott and L. Radom, *J. Phys. Chem.*, 1996, **100**, 16502–16513.
60 S. Khan, S. Khan, L. Khan, A. Farooq and A. M. Asiri, Fourier Transform Infrared Spectroscopy: Fundamentals and Application in Functional Groups and Nanomaterials Characterization, *Handbook of Materials Characterisation*, 2018, pp. 317–344.
61 G. M. Greetham, P. Burgos, Q. Cao, I. P. Clark, P. S. Codd, R. C. Farrow, M. W. George, M. Kogimtzis, P. Matousek, A. W. Parker, M. R. Pollard, D. A. Robinson, Z.-J. Xin and M. Towrie, *Appl. Spectrosc.*, 2010, **64**, 1311–1319.
62 D. Nečas and P. Klapetek, *Cent. Eur. J. Phys.*, 2011, **10**, 181–188.
63 K. Momma and F. Izumi, *J. Appl. Crystallogr.*, 2011, **44**, 1272–1276.